energies

MDPI

Article

Capacity Optimization Configuration of Hybrid Energy Storage Systems for Wind Farms Based on Improved k-means and Two-Stage Decomposition

Xi Zhang [1], Longyun Kang [1,2,*], Xuemei Wang [1,*], Yangbo Liu [1] and Sheng Huang [1]

[1] School of Electric Power, South China University of Technology, Guangzhou 510641, China; 202221015287@mail.scut.edu.cn (X.Z.); liuyb2@csg.cn (Y.L.); 202221015266@mail.scut.edu.cn (S.H.)
[2] College of New Energy, Longdong University, Qingyang 745000, China
* Correspondence: lykang@scut.edu.cn (L.K.); epxmwang@scut.edu.cn (X.W.)

Abstract: To address the issue of excessive grid-connected power fluctuations in wind farms, this paper proposes a capacity optimization method for a hybrid energy storage system (HESS) based on wind power two-stage decomposition. First, considering the susceptibility of traditional k-means results to initial cluster center positions, the k-means++ algorithm was used to cluster the annual wind power, with the optimal number of clusters determined by silhouette coefficient and Davies–Bouldin Index. The overall characteristics of each cluster and the cumulative fluctuations were considered to determine typical daily data. Subsequently, improved complete ensemble empirical mode decomposition with adaptive noise (ICEEMDAN) was used to decompose the original wind power data for typical days, yielding both the grid-connected power and the HESS power. To leverage the advantages of power-type and energy-type storage while avoiding mode aliasing, the improved pelican optimization algorithm—variational mode decomposition (IPOA-VMD) was applied to decompose the HESS power, enabling accurate distribution of power for different storage types. Finally, a capacity optimization model for a HESS composed of lithium batteries and supercapacitors was developed. Case studies showed that the two-stage decomposition strategy proposed in this paper could effectively reduce grid-connected power fluctuations, better utilize the advantages of different energy storage types, and reduce HESS costs.

Keywords: power fluctuations; hybrid energy storage system; k-means++; improved complete ensemble empirical mode decomposition with adaptive noise; variational mode decomposition; improved pelican optimization algorithm

Academic Editors: Raffaello Cozzolino and Gino Bella

Received: 15 January 2025
Revised: 5 February 2025
Accepted: 6 February 2025
Published: 8 February 2025

Citation: Zhang, X.; Kang, L.; Wang, X.; Liu, Y.; Huang, S. Capacity Optimization Configuration of Hybrid Energy Storage Systems for Wind Farms Based on Improved k-means and Two-Stage Decomposition. *Energies* **2025**, *18*, 795. https://doi.org/10.3390/en18040795

1. Introduction

With the increasingly severe issue of global climate change, reducing carbon emissions has become a global consensus and an urgent task. Wind energy, as a clean and renewable energy source, has gradually become a key force in the global energy transition because of its environmental friendliness and abundant resources [1]. Renewable energy, represented by wind power, has experienced rapid development in recent years, especially driven by technological innovations and large-scale applications. The cost of wind power generation has significantly decreased, its efficiency has continuously improved, and it has gradually gained the ability to compete with traditional fossil fuels. However, because of the randomness and volatility of wind power, a series of challenges have arisen to the safe and stable operation of the power system, requiring higher levels of system flexibility, load

matching, and other adjustments [2]. To meet the safety and technical requirements of the grid, countries have set clear limits on the fluctuations of wind farm grid integration, as shown in Table 1, requiring that the active power variations of wind generation within a certain time scale should not exceed the specified limits to ensure the safety and stability of the power system.

Table 1. Wind power grid integration standards for different countries.

Country	Wind Power Grid Integration Standards
United States	The 1 min ramp-up rate is less than 10% of the installed capacity
Canada	The 1 min ramp-up rate is less than 10% of the installed capacity
Denmark	The 1 min ramp-up rate is less than 5% of the installed capacity
Germany	At startup, the 1 min ramp-up rate is less than 10% of the installed capacity
United Kingdom	The 1 min variation is less than 10 MW, and the 1 min average ramp-up rate must not exceed three times the 10 min average ramp-up rate
China	Installed capacity < 30 MW: Variation within 10 min is less than 10 MW, and variation within 1 min is less than 3 MW Installed capacity 30–150 MW: Variation within 10 min is less than 1/3, and variation within 1 min is less than 1/10 Installed capacity > 150 MW: Variation within 10 min is less than 50 MW, and variation within 1 min is less than 15 MW

Traditional thermal power units, because of limitations such as startup and shutdown times and ramp-up rates, have difficulty effectively responding to the rapid changes and random fluctuations caused by wind power generation [3]. However, the rapid development of energy storage technology in recent years has provided crucial technical support to address this issue. The hybrid energy storage system (HESS) composed of lithium batteries and supercapacitors, with its flexible charging and discharging and fast response speed, has been proven to have significant effects in smoothing wind power fluctuations [4]. By deploying energy storage stations on the generation side, the active power fluctuations at wind power grid connection points can be effectively smoothed. However, the huge initial investment cost remains the main factor limiting its large-scale application. Therefore, the capacity optimization of the HESS, while ensuring compliance with wind power fluctuation requirements, urgently requires further in-depth research and discussion.

Scholars have proposed numerous effective methods for addressing uncertain variables in power systems. Reference [5] proposed a wind energy scenario generation method based on spatiotemporal covariance functions. Reference [6] combined stochastic programming and rolling horizon methods to design a two-stage operational structure based on copula to address various uncertainties of onboard multienergy loads and renewable energy. Reference [7] established an intraday correction method based on an opportunity-constrained model and multiagent deep reinforcement learning to determine a revised scheduling plan, addressing the uncertainty of renewable energy generation. In the research on energy storage system capacity optimization, because of the time-varying and uncertain nature of wind power data, directly utilizing all data for optimization is both complex and difficult to achieve. Therefore, using typical-day data has become an effective solution [8]. Typical-day data significantly reduce the amount of data required for optimization calculations, thus lowering computational costs and time. Furthermore, typical-day data can represent the characteristics of the power system during different periods, facilitating long-term planning. Currently, commonly used clustering analysis algorithms include k-means [9], fuzzy C-means (FCM) [10], and hierarchical clustering (HC) [11]. The k-means algorithm is known for its efficiency, ease of implementation, and wide applicability, but it is susceptible to the initial centroid position and is sensitive to noisy data.

Currently, research on wind power fluctuation smoothing has made some progress, with the main methods involving wavelet decomposition (WD), the moving average (MA) algorithm, empirical mode decomposition (EMD), and variational mode decomposition (VMD) to decompose wind power and extract fluctuation signals. Reference [12] used the MA algorithm to determine the grid-connected power and fluctuating power to be smoothed by the HESS, but it introduced time delays, and the energy storage system may not respond in time to sudden changes in wind power. Reference [13] used WD to separate high- and low-frequency power components, but the choice of wavelet basis and decomposition level influences the result of the wavelet transform. At the same time, WD denoising can produce pseudo-Gibbs phenomena. Reference [14] utilized model predictive control to obtain the wind power and the power of HESS. However, because of its high computational complexity, it may be difficult for this method to adjust quickly under rapidly changing wind conditions. Unlike traditional linear methods such as MA and WD, EMD and its variants are more suitable for processing nonlinear and nonstationary signals such as wind power [15]. However, EMD is prone to mode mixing, which leads to unclear decomposition results.

To fully leverage the complementary advantages of energy-type and power-type energy storage, a reasonable distribution of HESS power is critical. Reference [16] used the discrete Fourier transform (DFT) to decompose imbalanced power, dividing the power fluctuations into high-frequency and low-frequency bands. However, the DFT may not effectively capture instantaneous changes and nonlinear characteristics for nonstationary, time-varying power fluctuations. Reference [17] used an adaptive MA to smooth wind power and applied EMD to divide internal power, selecting the boundary point with minimal mode mixing. Although EMD can effectively decompose signals into multiple modes, mode mixing is likely to occur when processing complex nonlinear signals. Reference [18] proposed a capacity configuration method based on VMD, which decomposes photovoltaic output into power that meets grid integration requirements, along with its high- and low-frequency components. However, in the VMD method in the literature, the number of modes K and the secondary penalty factor α are often subjectively determined based on empirical values, which can lead to unreasonable decomposition and affect the smoothing effect. Reference [19] used particle swarm optimization (PSO) to search for the optimal parameter combination for VMD, enabling automatic parameter adjustment for power data with different characteristics. However, PSO is prone to getting stuck in local optima.

Considering the deficiencies in the above studies, the framework of this paper is shown in Figure 1. First, the k-means++ algorithm was used to cluster the wind power data for the entire year, determining the output of each typical day scenario based on the magnitude of the fluctuations. Improved complete ensemble empirical mode decomposition with adaptive noise (ICEEMDAN) was then applied to decompose the original wind power signal into grid-connected power and HESS power. Next, the improved pelican optimization algorithm (IPOA) was used to optimize the number of modes K and the penalty factor α in VMD, adaptively adjusting the parameters to decompose HESS power and accurately allocate internal HESS power. Finally, a HESS capacity optimization configuration model was established, and the model was solved based on typical-day data to determine the optimal configuration scheme for the HESS.

The innovations and advantages of this paper can be summarized in the following three aspects:

1. A novel method for selecting typical daily wind farm output based on an improved k-means is proposed. This method optimizes initial centroids using k-means++ and determines the optimal number of clusters through the silhouette coefficient (SC) and the Davies–Bouldin index (DBI). A typical-day selection mechanism is established based on cluster centroid distances and cumulative fluctuation magnitudes, overcom-

ing the limitation of traditional methods that rely solely on mean values to select representative scenarios, making the selected typical days more suitable for wind power fluctuation smoothing.

2. A power allocation strategy based on ICEEMDAN and IPOA-VMD is proposed. Compared with conventional PSO and POA, IPOA demonstrated superior search speed and optimization accuracy, enhancing the mode-matching accuracy of VMD. By leveraging the coordinated compensation of supercapacitors and lithium batteries, the proposed strategy reduced the occurrences of grid power fluctuation exceeding limits to zero at both 1 min and 10 min time scales, significantly improving wind power fluctuation smoothing and optimizing the overall performance of the HESS.
3. A HESS capacity optimization model based on typical daily data was developed. Case study analysis showed that, compared with conventional strategies, the proposed approach increased the wind power fluctuation qualification rate to 100% while reducing the annualized cost of the HESS by 7.79%, providing valuable engineering insights for HESS capacity planning.

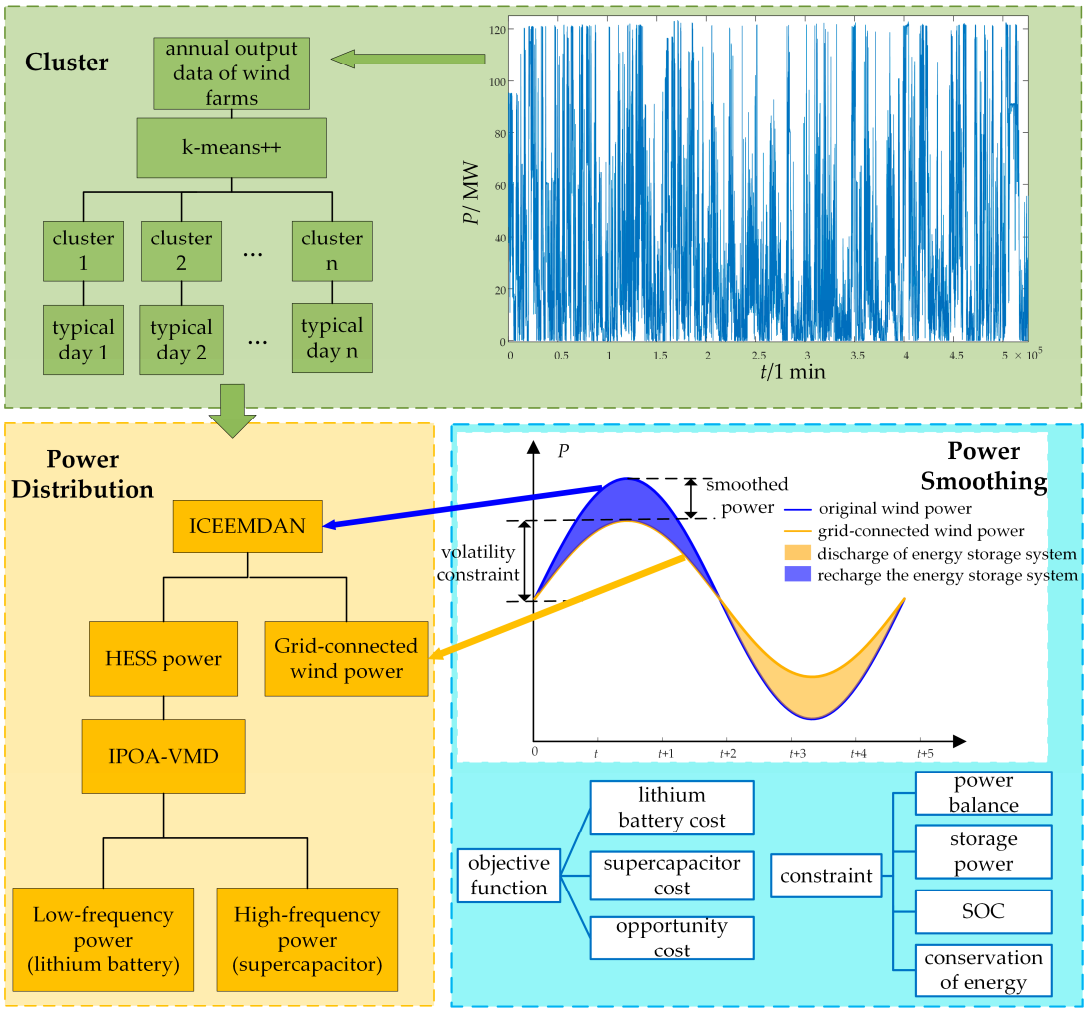

Figure 1. Thesis framework diagram.

2. Methodology

2.1. Method for Selecting Typical Days of Wind Power Based on k-means++

2.1.1. k-means++ Clustering Algorithm

The k-means algorithm is characterized by its speed, simplicity, and ease of understanding, and it remains widely used. However, the initial clustering centers of this

algorithm are chosen randomly, and different initial centers may lead to varying clustering results, slow convergence, or even clustering errors. To address this, Arthur et al. proposed the k-means++ algorithm [20], which modifies the method for selecting initial cluster centers. The algorithm proceeds as follows:

1. Randomly select a sample point from the dataset as the initial cluster center c.
2. Calculate the shortest Euclidean distance between each sample point and the existing cluster centers, denoted as $d(x)$.
3. Calculate the probability of each sample being selected as the next cluster center, $d^2(x)/\sum_{x\in X} d^2(x)$, and use the roulette method to choose the next cluster center.
4. Repeat steps 2 and 3 until k cluster centers are selected.
5. For each sample in the dataset, calculate the Euclidean distance to the k cluster centers, and assign it to the class corresponding to the closest cluster center.
6. For each class, recalculate its cluster center.
7. Repeat steps 5 and 6 until the cluster centers no longer change.

2.1.2. Selection of the Optimal Number of Clusters

Since the number of clusters in the k-means algorithm is predefined, the determination of the cluster number k is crucial for the quality of clustering analysis [21]. Therefore, this paper used the SC and DBI to determine the optimal number of clusters.

The SC considers both the cohesion and separation of sample data. For a sample z in the dataset, assume that it is clustered into class C. Its SC s_i is defined as:

$$s_i = \frac{b_i - a_i}{\max(a_i, b_i)} \tag{1}$$

In the equation, a_i represents the average distance between sample z_i and other samples within the same cluster, indicating the cohesion of the data within the cluster, and b_i represents the average distance between sample z_i and the nearest sample from other clusters, indicating the separation between clusters.

For a given clustering of the dataset, its SC s_k is defined as:

$$s_k = \frac{1}{n}\sum_{i=1}^{n} s_i \tag{2}$$

where n is the number of samples in the dataset and k is the number of clusters. s_k is also referred to as the average SC.

The SC s_i of sample z_i can be used to evaluate whether the sample fits well within its cluster. Since s_i ranges from -1 to 1, if s_i is close to 1, it indicates that the average distance a_i within the cluster is much smaller than the minimum average distance b_i between clusters, suggesting a correct clustering for this sample. Conversely, if s_i is close to -1, the sample is more suitable for the nearest other cluster.

For all k within the specified range, when the clustering SC s_k reaches its maximum value, the corresponding k is considered the optimal number of clusters.

The DBI, also known as the classification accuracy index, was proposed by David L. Davies and Donald Bouldin as a measure for evaluating the effectiveness of clustering algorithms [22]. The formula for calculating DBI is as follows:

$$\mathrm{DBI} = \frac{1}{k}\sum_{i=1}^{k} \max\left(\frac{\overline{C}_i + \overline{C}_j}{M_{i,j}}\right) \tag{3}$$

where $\overline{C}_i$ and $\overline{C}_j$ are the average sum of the distances between each scene in a different scenario cluster and its typical scene, and the distance between the typical scenes of clusters

i and j is denoted. A smaller DBI value indicates greater separation between the clusters and better clustering performance.

2.1.3. Rules for Selecting Typical Days

To determine the optimal number of clusters, this study comprehensively considered the SC and DBI and applied the k-means++ clustering algorithm to wind power data. Considering the need to smooth wind power fluctuations on typical days for subsequent analysis, the selection of typical days was based on a balance between cluster centroid proximity and volatility. The specific steps were as follows:

1. Compute the Euclidean distance d_i of each sample z_i from its cluster centroid c_i and the cumulative fluctuations B_i of sample z_i. Here, the fluctuations are defined as the differences between consecutive one-minute power datapoints, and the value of cumulative fluctuations is the sum of all fluctuations over a day.
2. Normalize the Euclidean distance d_i and cumulative fluctuations B_i for each sample, introducing a weight coefficient γ ($0 < \gamma < 1$).
3. Calculate the comprehensive weight w_i for each sample as $w_i = \gamma d_i / d_{\max} - (1-\gamma) B_i / B_{\max}$, where $d_{\max}$ and $B_{\max}$ are the maximum Euclidean distance and maximum cumulative fluctuations among all samples, respectively.
4. Select the sample with the smallest comprehensive weight w_i in each cluster as the typical day data for that cluster.

2.2. Power Distribution Strategy

2.2.1. ICEEMDAN

To address the reconstruction errors and modal aliasing issues of traditional EMD and ensemble empirical mode decomposition (EEMD) [23], ICEEMDAN was used to decompose the wind power. The steps were as follows:

Define P as the wind power signal to be decomposed, $E(q)$ as the q-th order mode component produced by EMD, $N(i)$ as the local mean of the signal, $W(i)$ as Gaussian white noise, and β_q as the standard deviation of white noise.

1. Add i groups of white noise $W(i)$ to the original wind speed series, resulting in:

$$P(i) = P + \beta_1 E(W(i)) \tag{4}$$

2. Calculate the envelope and obtain the first residual component and the first modal component by averaging:

$$R_1 = \beta_1 N(P(i)) \tag{5}$$

$$\mathrm{IMF}_1 = P - R_1 \tag{6}$$

3. Continue adding white noise and use local mean decomposition to calculate the q-th order residual and the q-th order modal component:

$$R_q = N(R_{q-1} + \beta_{q-1} E(W(i))) \tag{7}$$

$$\mathrm{IMF}_q = R_{q-1} - R_q \tag{8}$$

4. Continue until the decomposition is completed, obtaining all the modes and residuals.

2.2.2. IPOA-VMD

VMD is a nonrecursive algorithm that first constructs a variational model, predefines the number of modes K and the quadratic penalty factor α, and then iteratively searches

for the optimal solution of the model, adaptively separating the signal into intrinsic modal functions (IMFs) [24]. The decomposition process is as follows:

1. Construct the variational problem. By applying the Hilbert transform to the input signal, the corresponding analytic signal is obtained. Multiplying it by the corresponding center frequency shifts the spectrum to the base frequency band, and Gaussian smoothing is used to adjust the bandwidth of the signal. The constrained variational model is:

$$\begin{cases} \min\limits_{\{u_k\},\{\omega_k\}} \left(\sum\limits_{k=1}^{K} \left\| \partial_i \left\{ \left[\delta(t) + \frac{j}{\pi t} \right] * u_k(t) \right\} e^{-j\omega_k t} \right\|_2^2 \right) \\ \text{s.t.} \sum\limits_{k=1}^{K} u_k(t) = f(t) \end{cases} \tag{9}$$

In the equation, * denotes the convolution operation; $\{u_k\} = \{u_1, u_2, \ldots, u_k\}$ represents all IMF components; $\{\omega_k\} = \{\omega_1, \omega_2, \ldots, \omega_k\}$ represents the center frequency of each IMF; and $\delta(t)$ represents the unit impulse function, $j = \sqrt{-1}$.

2. Reconstruct the constrained problem. To solve the above problem, a quadratic penalty term is used to penalize the violation of the constraints, transforming the constrained problem into an unconstrained problem. The augmented Lagrange function operator λ and the penalty factor α are introduced to complete the reconstruction of the problem, which is represented as:

$$\begin{aligned} L(\{u_k\}, \{\omega_k\}, \lambda(t)) = \alpha \sum_{k=1}^{K} \left\| \partial_i \left\{ \left[\delta(t) + \frac{j}{\pi t} \right] * u_k(t) \right\} e^{-j\omega_k t} \right\|_2^2 \\ + \left\| f(t) - \sum_{k=1}^{K} u_k(t) \right\|_2^2 + \left\langle \lambda(t), f(t) - \sum_{k=1}^{K} u_k(t) \right\rangle \end{aligned} \tag{10}$$

3. Solve the unconstrained problem. The optimal solution of the problem is searched through a frequency-domain iterative method. Using the alternating direction method of multipliers, the components $u_k(t)$, center frequencies ω_k, and Lagrange multipliers are iteratively updated until the stopping conditions are met. The update process and iteration stopping expressions are shown in Equations (11) and (12).

$$\lambda^{n+1}(\omega) = \lambda^n(\omega) + \tau[f(\omega) - \sum_{k=1}^{K} u_k^{n+1}(\omega)] \tag{11}$$

$$\sum_{k=1}^{K} \frac{\left\| u_k^{n+1}(\omega) - u_k^n(\omega) \right\|_2^2}{\left\| u_k^n(\omega) \right\|_2^2} < \varepsilon \tag{12}$$

In the equation, τ is the noise tolerance parameter and ε is the convergence accuracy, where $\varepsilon > 0$.

The decomposition performance of VMD depends on the number of modes K and the penalty factor α. Appropriate values of K and α can improve the signal decomposition performance. POA has advantages such as fast optimization speed, fewer parameters, high convergence accuracy, ease of operation, and wide applicability [25]. However, this algorithm tends to experience slower convergence speed and may get stuck in local optima in the later stages of iteration.

Therefore, this paper proposes an IPOA that combines logistic chaotic mapping strategy and Lévy flight to effectively avoid the shortcomings of getting stuck in local optima. It also allows automatic adjustment of the VMD algorithm's parameters K and α based on different wind power signals, improving decomposition accuracy and adaptability. The specific improvements are as follows.

1. Logistic chaotic mapping strategy [26]

As the number of iterations of the POA increases, the diversity of the pelican population decreases. Introducing logistic chaotic mapping to initialize the pelican population can effectively improve the quality of the initial solution, thereby increasing the diversity of the pelican population and improving the convergence speed and accuracy of the algorithm as a whole.

The formula for logistic chaotic mapping is:

$$Y_{n+1} = aY_n(1-Y_n) \tag{13}$$

where $Y_n \in [0, 1]$, $a \in [0, 4]$.

In the logistic chaotic mapping, when a is closer to 4, Y becomes closer to the uniform distribution in [0, 1]. When a = 4, it exhibits a completely chaotic state, with a uniform mapping distribution at the limit.

2. Development stage position optimization based on Lévy flight

Lévy flight is a walk that alternates between short-range searches and random longer-distance movements, simulating the random walk process of animals searching for food in nature [27].

The random step length formula is:

$$s = \frac{\mu}{|v|^{\frac{1}{\beta}}} \tag{14}$$

where s is the walk step length; β is a parameter with a value of 1.5; and μ and v are direction vectors following a normal distribution, with standard deviations:

$$\sigma_\mu = \left[\frac{\Gamma(1+\beta) \times \sin(\pi \times \frac{\beta}{2})}{\Gamma(1+\frac{\beta}{2}) \times \beta \times 2}\right]^{\frac{1}{\beta}}, \sigma_v = 1 \tag{15}$$

During each iteration of the algorithm, the development stage performs Lévy flight mutation operations on individuals in the population. If the fitness of the mutated individual is better than before, the new position is retained; otherwise, the original position is kept. The specific position update formula is:

$$x_{i,j}^{P2} = x_{i,j} \times s + 0.2 \times (1 - \frac{N_{\text{iter}}}{N_{\max}}) \times (2 \times \text{rand} - 1) \times x_{i,j} \tag{16}$$

In the equation, $x_{i,j}^{P2}$ represents the updated value of the j-th variable for the i-th candidate solution at the development stage; N_{iter} denotes the current iteration number; and $N_{\max}$ denotes the maximum number of iterations.

This paper used the IPOA, with envelope entropy as the fitness function, to optimize the modal number K and penalty factor α of VMD, with specific parameters shown in Appendix A Table A1. The flowchart of the IPOA-VMD is shown in Figure 2.

2.2.3. Power Distribution Strategy Based on Two-Stage Decomposition

The typical daily wind power data selected in Section 2.1 was decomposed using ICEEMDAN, yielding various IMFs. Since processing each IMF component individually would result in unnecessary workload, they were reconstructed into low-frequency and high-frequency components by combining the wind power grid-connected fluctuation limits. The low-frequency component was directly connected to the grid, while the high-frequency component was assigned as the HESS power, as shown in the following equation:

$$P_{\text{wind},n} = P_{\text{grid},n} + P_{\text{HESS},n} \tag{17}$$

In the equation, $P_{\text{wind},n}$, $P_{\text{grid},n}$, and $P_{\text{HESS},n}$ represent the original wind power signal, the direct grid-connected power, and the HESS power, respectively, at the n-th moment.

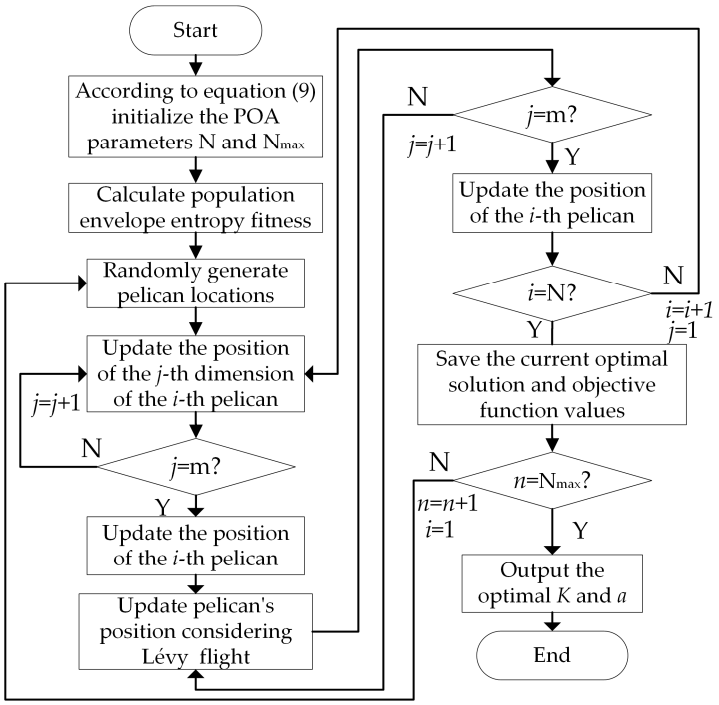

Figure 2. Flowchart for IPOA-VMD.

The reconstruction of IMF involves summing the components of the low-frequency and high-frequency bands according to the given criteria to obtain the low-frequency and high-frequency components. The reconstruction methods are divided into high-frequency reconstruction (fine to coarse, f2c) and low-frequency reconstruction (coarse to fine, c2f) [28]. High-frequency reconstruction generates each high-frequency reconstructed component by summing the results of EMD from top to bottom. Low-frequency reconstruction generates each low-frequency reconstructed component by summing the results of ICEEMDAN from bottom to top. The reconstruction method is shown in the following equation:

$$\begin{cases} \text{c2f}(1) = \text{res} \\ \text{c2f}(2) = \text{res} + \text{IMF}q \\ \vdots \\ \text{c2f}(q{+}1) = \text{res} + \text{IMF}q + \ldots + \text{IMF1} \end{cases} \tag{18}$$

After obtaining the HESS power, IPOA-VMD was used to decompose the HESS power into K modal components and the residual. Based on the degree of aliasing and amplitude of the IMF components obtained from IPOA-VMD, the frequency boundary between high and low frequencies was determined. The high and low frequency signals were then reconstructed and sequentially allocated to the supercapacitor and lithium battery, as shown in the following equation:

$$\begin{cases} P_{\text{Li}} = \sum_{k=1}^{\text{m}} P_k \\ P_{\text{sc}} = \sum_{k=g+1}^{K-1} P_k + \text{res} \end{cases} \tag{19}$$

In the equation, P_{Li} and P_{sc} represent the power allocated to the lithium battery and the supercapacitor in the HESS, respectively; P_k denotes the k-th order IMF component decomposed by NGO-VMD, and g is the cutoff point between high and low frequencies in the VMD. The final power allocation flowchart based on the two-stage decomposition is shown in Figure 3.

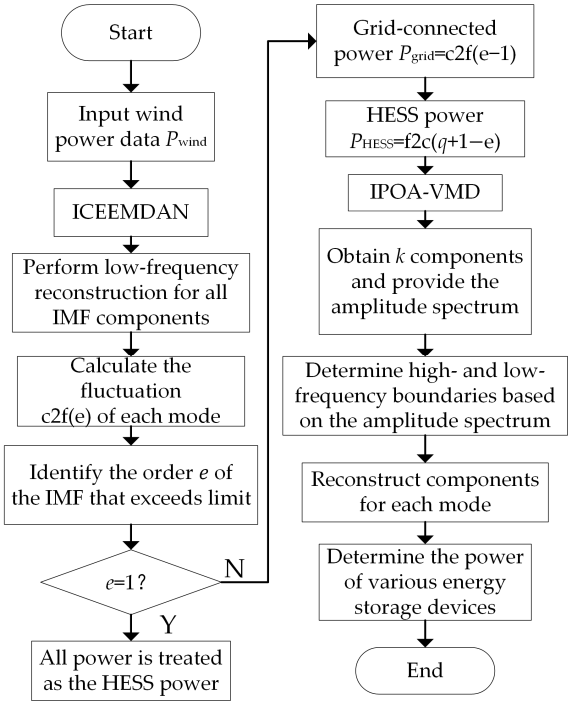

Figure 3. Power allocation flowchart based on the two-stage decomposition.

2.3. HESS Capacity Optimization Configuration

Based on the grid-connected power and HESS power distribution strategy proposed in Section 2.2, a HESS capacity optimization configuration model was established, considering wind power fluctuations smoothing. The structure diagram of the wind-storage power generation system is shown in Figure 4 [29].

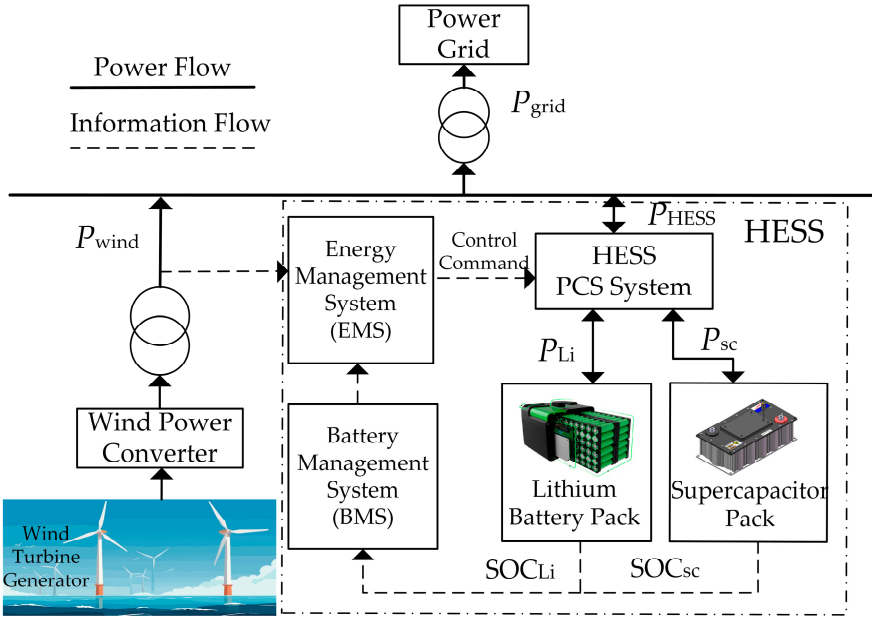

Figure 4. Structure of wind-storage power generation system.

2.3.1. Objective Function

The objective function, consisting of lithium battery cost, supercapacitor cost, and wind power fluctuation opportunity compensation cost, is shown in Equation (20).

$$\min C = C_{\mathrm{Li}} + C_{\mathrm{sc}} + C_{\mathrm{comp}} \tag{20}$$

In the equation, C is the annual total cost; C_{Li} is the lithium battery storage cost; C_{sc} is the supercapacitor cost; and C_{comp} is the wind power fluctuation opportunity compensation cost.

C_{Li} and C_{sc} are given by the following equations:

$$C_{\mathrm{Li}} = C_{\mathrm{Li}}^{\mathrm{inv}} + C_{\mathrm{Li}}^{\mathrm{oper}} - C_{\mathrm{Li}}^{\mathrm{re}} \tag{21}$$

$$C_{\mathrm{sc}} = C_{\mathrm{sc}}^{\mathrm{inv}} + C_{\mathrm{sc}}^{\mathrm{oper}} - C_{\mathrm{sc}}^{\mathrm{re}} \tag{22}$$

In the equations, $C_{\mathrm{Li}}^{\mathrm{inv}}$, $C_{\mathrm{Li}}^{\mathrm{oper}}$, and $C_{\mathrm{Li}}^{\mathrm{re}}$ represent the investment cost, operation and maintenance (O&M) cost, and residual value, respectively, of the lithium battery, and $C_{\mathrm{sc}}^{\mathrm{inv}}$, $C_{\mathrm{sc}}^{\mathrm{oper}}$, and $C_{\mathrm{sc}}^{\mathrm{re}}$ represent the investment cost, O&M cost, and residual value, respectively, of the supercapacitor.

1. Investment Cost:

$$C_{\mathrm{Li}}^{\mathrm{inv}} = (c_{\mathrm{Li,P}}^{\mathrm{inv}} P_{\mathrm{Li}} + c_{\mathrm{Li,E}}^{\mathrm{inv}} E_{\mathrm{Li}}) \frac{\mathrm{r}(1+\mathrm{r})^{\mathrm{Y_{Li}}}}{(1+\mathrm{r})^{\mathrm{Y_{Li}}} - 1} \tag{23}$$

$$C_{\mathrm{sc}}^{\mathrm{inv}} = (c_{\mathrm{sc,P}}^{\mathrm{inv}} P_{\mathrm{sc}} + c_{\mathrm{sc,E}}^{\mathrm{inv}} E_{\mathrm{sc}}) \frac{\mathrm{r}(1+\mathrm{r})^{\mathrm{Y_{sc}}}}{(1+\mathrm{r})^{\mathrm{Y_{sc}}} - 1} \tag{24}$$

In the equations, $c_{\mathrm{Li,P}}^{\mathrm{inv}}$ and $c_{\mathrm{Li,E}}^{\mathrm{inv}}$ are the investment cost coefficients for the power and capacity of the lithium battery, respectively; $c_{\mathrm{sc,P}}^{\mathrm{inv}}$ and $c_{\mathrm{sc,E}}^{\mathrm{inv}}$ are the investment cost coefficients for the power and capacity of the supercapacitor, respectively; r is the discount rate; and $\mathrm{Y_{Li}}$ and $\mathrm{Y_{sc}}$ are the operating lifetimes of the lithium battery and supercapacitor, respectively.

2. O&M Cost:

O&M cost was estimated based on the proportion of the investment cost [30], as shown in the following equations:

$$C_{\mathrm{Li}}^{\mathrm{oper}} = \mathrm{a_{Li}} C_{\mathrm{Li}}^{\mathrm{inv}} \tag{25}$$

$$C_{\mathrm{sc}}^{\mathrm{oper}} = \mathrm{a_{sc}} C_{\mathrm{sc}}^{\mathrm{inv}} \tag{26}$$

In the equations, $\mathrm{a_{Li}}$ and $\mathrm{a_{sc}}$ represent the proportions of the O&M costs to the investment costs for the lithium battery and supercapacitor, respectively.

3. Residual Value:

$$C_{\mathrm{Li}}^{\mathrm{re}} = (c_{\mathrm{Li,P}}^{\mathrm{inv}} P_{\mathrm{Li}} + c_{\mathrm{Li,E}}^{\mathrm{inv}} E_{\mathrm{Li}}) \frac{\mathrm{b_{Li}} \cdot \mathrm{r}}{(1+\mathrm{r})^{\mathrm{Y_{Li}}} - 1} \tag{27}$$

$$C_{\mathrm{sc}}^{\mathrm{re}} = (c_{\mathrm{sc,P}}^{\mathrm{inv}} P_{\mathrm{sc}} + c_{\mathrm{sc,E}}^{\mathrm{inv}} E_{\mathrm{sc}}) \frac{\mathrm{b_{sc}} \cdot \mathrm{r}}{(1+\mathrm{r})^{\mathrm{Y_{sc}}} - 1} \tag{28}$$

In the equations, $\mathrm{b_{Li}}$ and $\mathrm{b_{sc}}$ represent the residual value rates of the lithium battery and supercapacitor, respectively.

4. Wind Power Fluctuation Opportunity Compensation Cost:

Because of the limitations of energy storage power and capacity, when wind power fluctuations are large, the HESS cannot fully meet the storage power task, requiring the dispatch of other flexibility resources in the power system, which increases operational costs [31]. The opportunity compensation cost was used to measure the additional operational costs caused by insufficient compensation, as shown in the following equation:

$$C_{\text{comp}} = \sum_{n=1}^{\text{N}} \text{c}_{\text{comp}}(P_{\text{posi},n} - P_{\text{nega},n}) \tag{29}$$

In the equation, C_{comp} is the opportunity compensation cost coefficient, and $P_{\text{posi},n}$ and $P_{\text{neg},n}$ represent the positive and negative undercompensation at the n-th time step, respectively.

2.3.2. Constraints

1. Power balance constraint

When the power task is a positive fluctuation, the system absorbs the fluctuating power by charging the lithium battery and supercapacitor. When the power task is a negative fluctuation, the system relies on discharging the lithium battery and supercapacitor to compensate for the fluctuating power.

$$P_{\text{HESS},n} = P_{\text{Li},n}^{\text{ch}} + P_{\text{sc},n}^{\text{ch}} + P_{\text{posi},n} - P_{\text{Li},n}^{\text{disc}} - P_{\text{sc},n}^{\text{disc}} - P_{\text{nega},n} \tag{30}$$

In the equation, $\text{P}_{\text{HESS},\,n}$ is the total power of the HESS at the n-th time step; $P_{\text{Li},n}^{\text{ch}}$ and $P_{\text{Li},n}^{\text{disc}}$ are the charging and discharging powers of the lithium battery at the n-th time step, respectively; and $P_{\text{sc},n}^{\text{ch}}$ and $P_{\text{sc},n}^{\text{disc}}$ are the charging and discharging powers of the supercapacitor at the n-th time step, respectively.

2. Charge–discharge power constraint

$$\begin{cases} |P_{\text{Li},n}| \le P_{\text{Li,N}} \\ |P_{\text{sc},n}| \le P_{\text{sc,N}} \end{cases} \tag{31}$$

3. Energy conservation constraint

$$\begin{cases} E_{\text{Li},n} = E_{\text{Li},n-1} + P_{\text{Li},n}\eta_{\text{Li,cha}} & ,P_{\text{Li},n} > 0 \\ E_{\text{sc},n} = E_{\text{sc},n-1} + P_{\text{sc},n}\eta_{\text{sc,cha}} & ,P_{\text{sc},n} > 0 \\ E_{\text{Li},n} = E_{\text{Li},n-1} + P_{\text{Li},n}/\eta_{\text{Li,disc}} & ,P_{\text{Li},n} \le 0 \\ E_{\text{sc},n} = E_{\text{sc},n-1} + P_{\text{sc},n}/\eta_{\text{sc,disc}} & ,P_{\text{sc},n} \le 0 \end{cases} \tag{32}$$

In the equation, $E_{\text{Li},n}$ and $E_{\text{Li},n-1}$ are the remaining capacities of the lithium battery at the n-th and $n-1$-th time steps, respectively; $E_{\text{sc},n}$ and $E_{\text{sc},n-1}$ are the remaining capacities of the supercapacitor at the n-th and $n-1$-th time steps, respectively; $\eta_{\text{Li,cha}}$ and $\eta_{\text{sc,cha}}$ are the charging efficiencies of the lithium battery and supercapacitor, respectively; and $\eta_{\text{Li,disc}}$ and $\eta_{\text{sc,disc}}$ are the discharging efficiencies of the lithium battery and supercapacitor, respectively.

4. SOC constraint

$$\begin{cases} \text{SOC}_{\text{Li,min}} \le \text{SOC}_{\text{Li},n} \le \text{SOC}_{\text{Li,max}} \\ \text{SOC}_{\text{sc,min}} \le \text{SOC}_{\text{sc},n} \le \text{SOC}_{\text{sc,max}} \end{cases} \tag{33}$$

In the equation, $SOC_{Li,min}$ and $SOC_{Li,max}$ are the lower and upper bounds, respectively, of the lithium battery's state of charge; $SOC_{sc,min}$ and $SOC_{sc,max}$ are the lower and upper bounds, respectively, of the supercapacitor's SOC; and $SOC_{Li,n}$ and $SOC_{sc,n}$ are the SOC of the lithium battery and supercapacitor at the n-th time step, respectively.

3. Discussion and Analysis of Experimental Results

3.1. Clustering to Generate Typical Days

k-means, k-means++, HC, and fuzzy C-means were applied to the actual 1 min wind power data from a 120 MW offshore wind farm in China over the entire year. The SCs and DBIs for different numbers of clusters are shown in Tables 2 and 3 below.

Table 2. Comparison of SCs.

Clustering Algorithm	k = 3	k = 4	k = 5	k = 6	k = 7
k-means	0.5824	0.3894	0.3941	0.3892	0.3708
k-means++	0.5800	0.6083	0.3864	0.3995	0.3904
HC	0.5858	0.5972	0.3829	0.3790	0.3892
FCM	0.4842	0.3852	0.3120	0.3147	0.2293

Table 3. Comparison of DBIs.

Clustering Algorithm	k = 3	k = 4	k = 5	k = 6	k = 7
k-means	1.2126	1.4144	1.3399	1.4631	1.5443
k-means++	1.2131	1.1435	1.3176	1.4487	1.5250
HC	1.3013	1.3178	1.3314	1.5222	1.5166
FCM	1.2948	1.4562	2.0640	1.8110	1.9965

From the above tables, it can be seen that when k = 4, the DBI value of the k-means++ was the smallest, indicating that the dispersion of the clusters was at its lowest. At the same time, the SC was the largest, indicating that the cluster centroids were closest within the same cluster and that the clustering effect was optimal.

The final number of clusters for k-means++ was determined to be 4, and the clustering results are shown in Figure 5. The different colored curves in the Figure 5 indicate different samples of daily wind power in each scenario. Scenario 1 exhibited significant intermittent power generation characteristics, with its daily power curve maintaining short periods of rated power output within the 24 h cycle. Scenario 2 demonstrated ideal continuous power generation characteristics, maintaining high power output for most of the day, with the curve shape matching the expected generation behavior under stable wind conditions. Scenario 3 featured a bimodal distribution, maintaining high power output during the first and last segments of the daily cycle while experiencing a significant power drop during the midday period. Scenario 4 exhibited an asymmetric generation pattern, with the main power peaks concentrated in the latter half of the daily cycle and intermittent short-term power fluctuations occurring during the early morning period. With the weight coefficient γ = 0.5, the typical-day curves for the four clusters are shown in Figure 6.

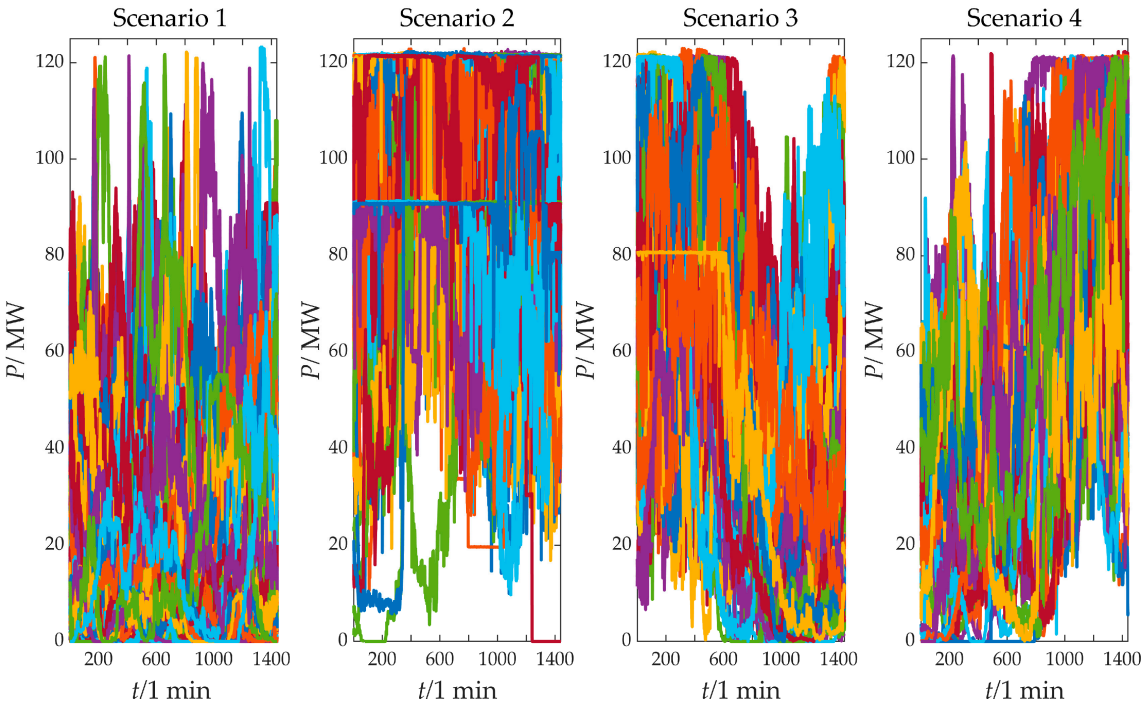

Figure 5. Results of k-means++ clustering.

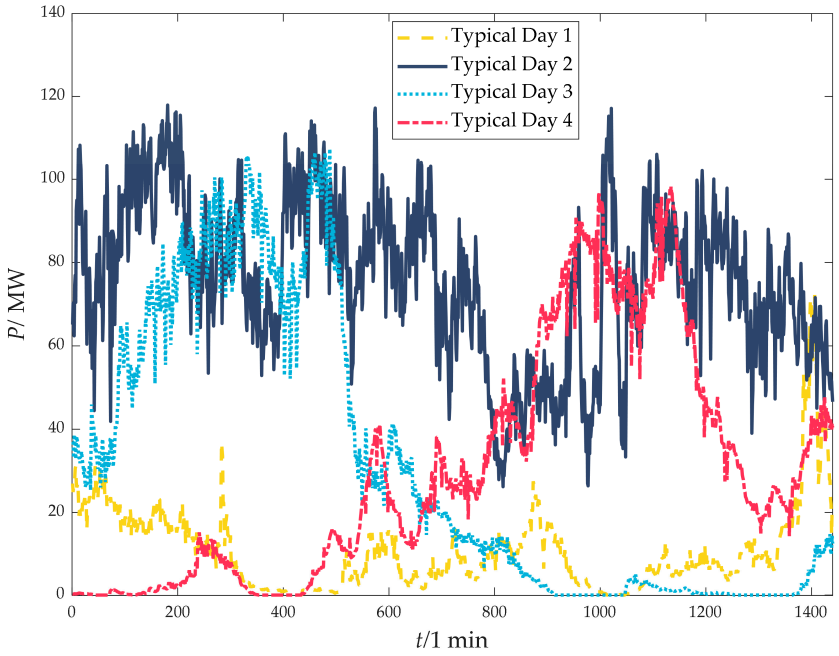

Figure 6. Typical daily wind power curves.

3.2. Power Distribution

Taking typical day 2 as an example, ICEEMDAN was used. According to China's wind power grid connection standard, the 1 min grid fluctuation limit is 1/10 of the installed capacity, which here was 12 MW. Using this as the high- and low-frequency boundary, low-frequency reconstruction yielded the grid-connected power and HESS power. The ICEEMDAN results and reconstruction results of each component are shown in Figures 7 and 8, respectively.

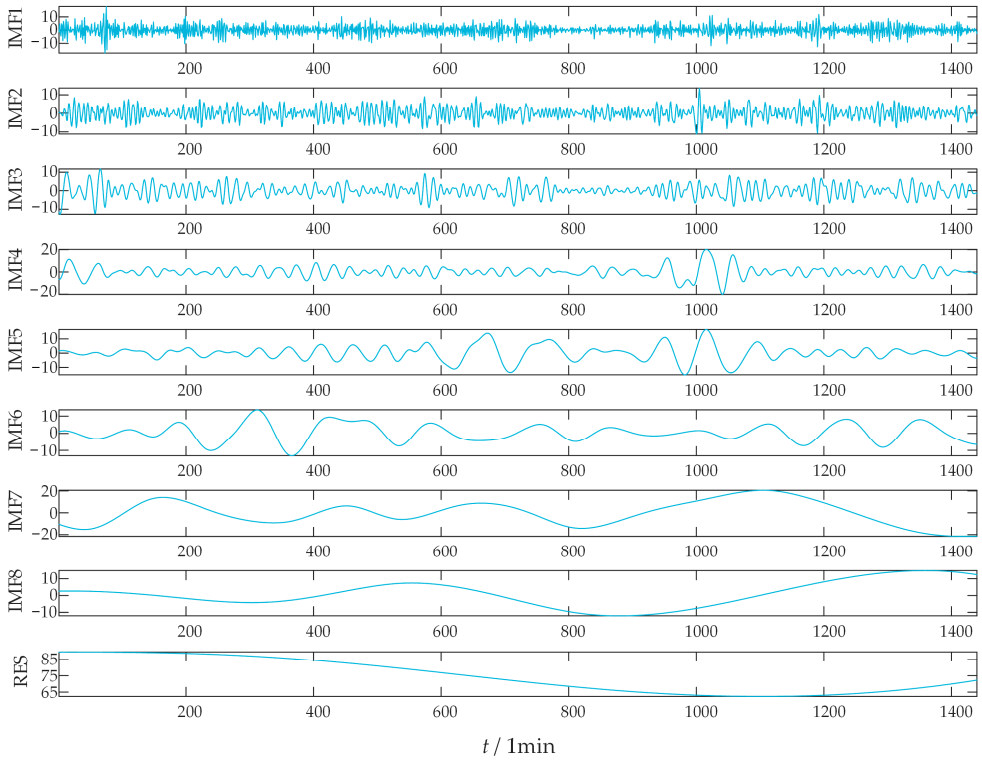

Figure 7. Results of ICEEMDAN.

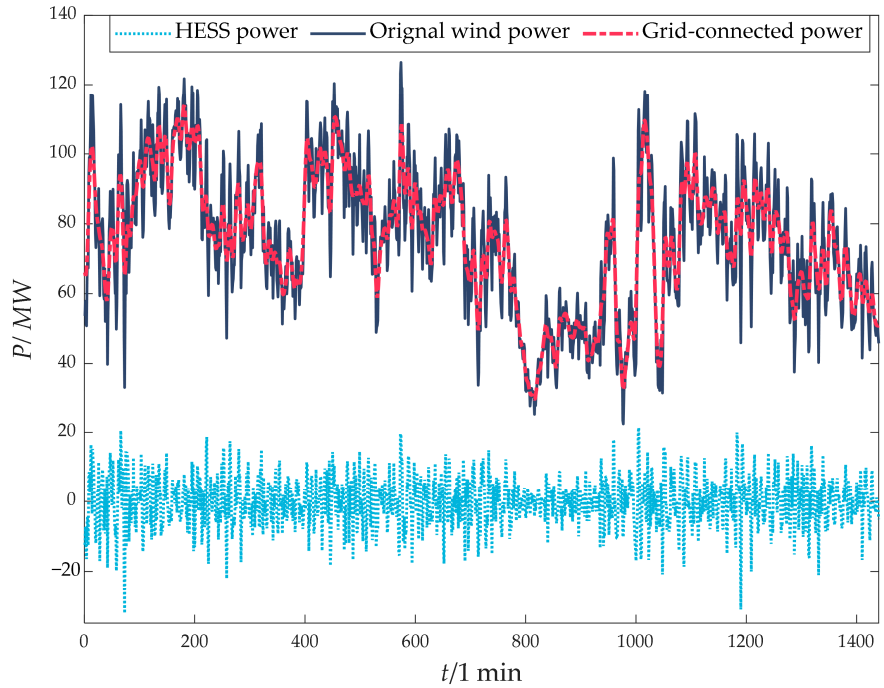

Figure 8. Reconstruction results of ICEEMDAN.

To verify the advantages of IPOA, IPOA, POA, and PSO were compared in optimizing the fitness of VMD parameters, using the HESS power on typical day 2 as an example. The iterative optimization process of the three algorithms is shown in Figure 9.

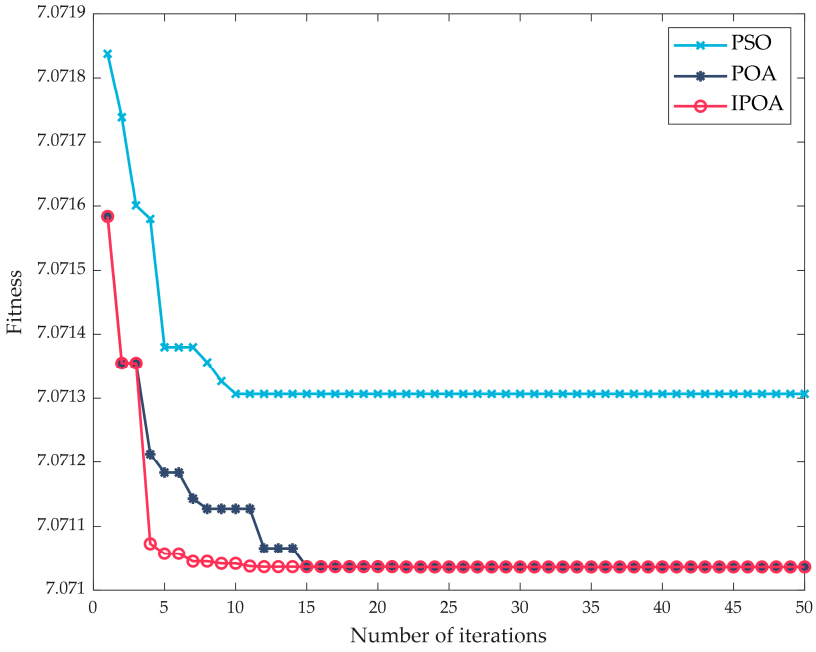

Figure 9. Iteration curve of the three algorithms.

From the above figure, it can be seen that the IPOA converged at the 11th iteration, achieving the minimum fitness value of 7.071037, whereas the POA converged to the same fitness value only at the 15th iteration. The PSO algorithm converged at the 10th generation, but its minimum fitness value was 7.071306, indicating the occurrence of local convergence. A comparison of the iterative curves showed that the IPOA outperformed the POA and PSO in convergence speed and effectively avoided local convergence.

The optimal K value obtained after IPOA optimization was 8, and the optimal penalty factor α value was 6214. To verify the advantages of VMD in suppressing mode mixing, VMD and EMD were applied to decompose the HESS power on typical day 1. The magnitude spectra of the two algorithms are shown in Figures 10 and 11.

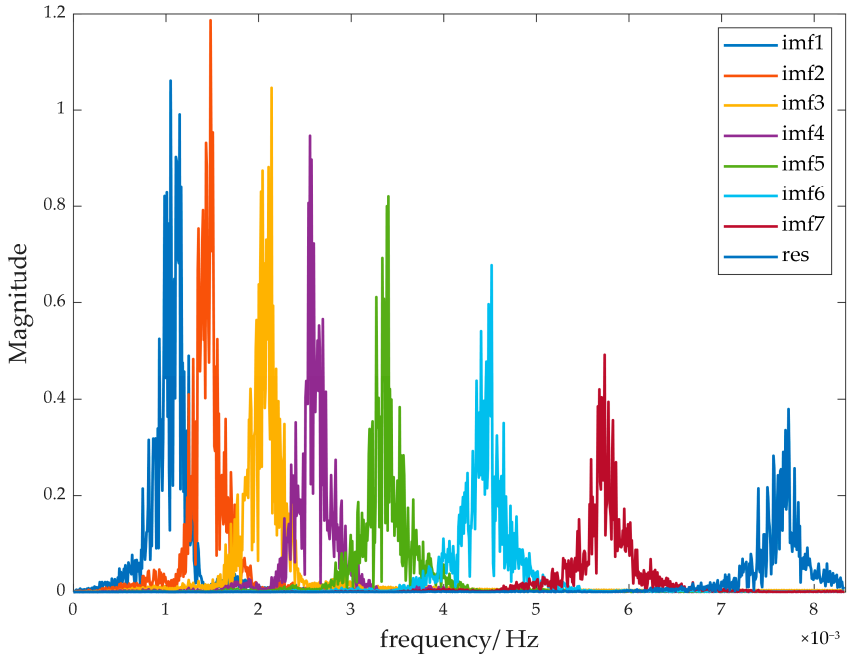

Figure 10. Magnitude spectrum of VMD.

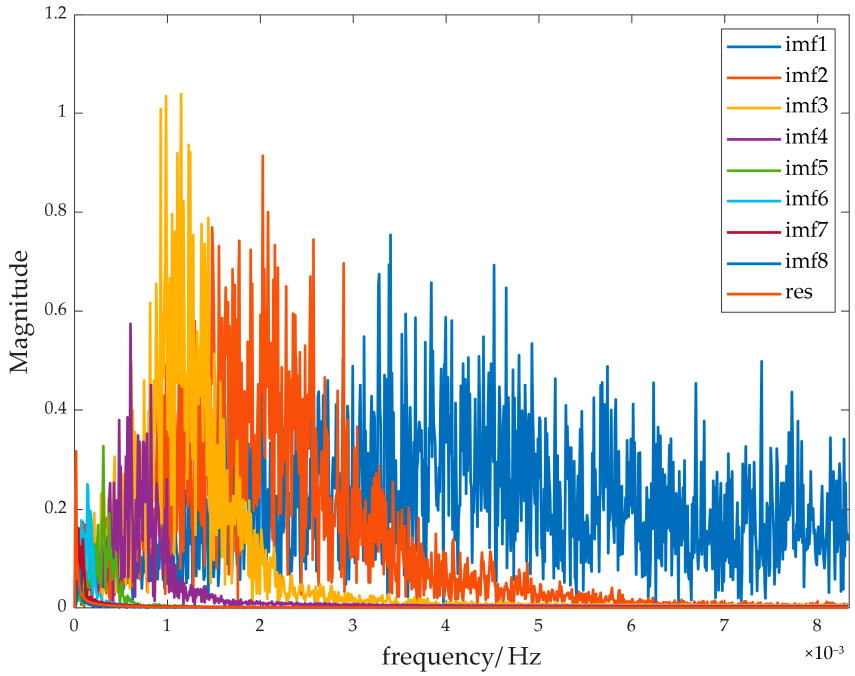

Figure 11. Magnitude spectrum of EMD.

From Figures 10 and 11, it can be seen that the components in the magnitude spectrum of EMD almost completely overlapped, which was unfavorable for internal power allocation in the HESS, while the overlapping parts of each IMF component in VMD were minimal. Therefore, based on the degree of overlap and the amplitude of each VMD component, imf1–imf5 were categorized as low-frequency components and assigned to lithium batteries, while imf6–res were categorized as high-frequency components and assigned to supercapacitors. The internal power allocation curve of the HESS is shown in Figure 12.

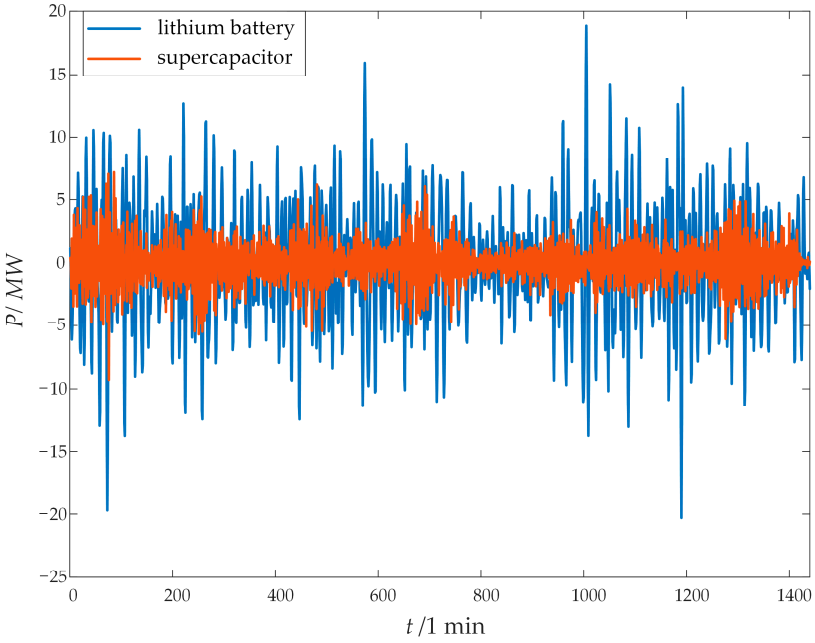

Figure 12. Distribution of power within the HESS.

3.3. Results of HESS Capacity Optimization Configuration

In this paper, the YALMIP toolbox and Gurobi solver were employed to solve the HESS capacity optimization configuration model. The specific solver parameter settings and model parameters are detailed in Appendix A, Tables A2 and A3, respectively.

To verify the smoothing effect of wind power, the following four schemes were designed:

Scheme 1: The MA algorithm was used to smooth wind power.

Scheme 2: EMD was used to smooth wind power.

Scheme 3: The IPOA-VMD was used to smooth wind power.

Scheme 4: ICEEMDAN was used to smooth wind power.

To avoid mode mixing and achieve accurate allocation of lithium battery power and supercapacitor power, IPOA-VMD was used to decompose HESS power in all four schemes. The results of the HESS configurations for the four schemes are shown in Table 4 below, using typical day 2 as an example.

Table 4. HESS capacity configuration results for the three schemes.

Parameters	Scheme 1	Scheme 2	Scheme 3	Scheme 4
Lithium battery power /MW	10.61761	7.476901	6.034713	7.361035
Lithium battery capacity/MW·h	0.5705331	1.382324	0.3252731	1.002809
Supercapacitor power/MW	5.513871	4.450731	3.938104	4.923756
Supercapacitor capacity/MW·h	0.123192	0.1467984	0.09366347	0.1449318
Investment cost/10 k CNY	606.0136	477.9401	357.9292	461.9565
O&M cost/10 k CNY	1.212027	9.558803	7.158584	9.516771
Recovery value/10 k CNY	49.07465	39.34212	29.18946	37.54483
Opportunity compensation cost/10 k CNY	123.6268	227.6628	319.11602	205.0725
Annualized total cost/10 k CNY	692.6860	682.9033	655.0143	638.7233

As shown in the table above, compared with the first three schemes, the annual comprehensive cost reduction for Scheme 4 was 7.79%, 6.47%, and 2.49%, respectively. From the HESS power and capacity configuration results, in the design of Scheme 1, the HESS power configuration was too large, leading to excessively high total costs. Meanwhile, the capacities of the lithium batteries and supercapacitors were relatively small, causing the system to frequently charge and discharge during wind power fluctuations, which impacted the HESS's lifespan and reliability. Scheme 3 had a smaller power and capacity configuration, and to compensate for the power shortfall, the system was forced to call on high-cost external power, resulting in the opportunity compensation cost accounting for 48.72% of the total cost. At the same time, because the heavy reliance on external power sources, when facing power fluctuations, the external backup power may not have been able to respond in time. In Schemes 2 and 4, the power and capacity configurations of the lithium batteries and supercapacitors were more balanced, especially in Scheme 4, where the HESS capacity configuration achieved the optimal balance between capacity and costs. Compared with Scheme 3, the opportunity compensation cost in Scheme 4 was reduced by 35.74%, ultimately achieving the lowest total cost.

Scheme 4 was used to configure the HESS capacity for four typical days, with results shown in Table 5. The maximum value of the configurations for all typical days was selected as the final HESS configuration plan.

Table 5. HESS configuration results for four typical days.

Typical Day	E_{Li}	P_{Li}	E_{sc}	P_{sc}
1	0.3553705	3.059701	0.04220754	1.502692
2	1.002809	7.361035	0.1449318	4.923756
3	0.3836545	7.436658	0.06125014	3.171559
4	0.2594061	4.601879	0.03802841	1.835683
Final configuration results	1.002809	7.436658	0.1449318	4.923756

3.4. Analysis of Wind Power Smoothing Effect

The smoothed fluctuations are key criteria for evaluating the smoothing effects of different schemes. The wind power fluctuations on the 1 min and 10 min scales before and after smoothing for Schemes 1–4 are shown in Figures 13–16, respectively. In Scheme 1, because of the small HESS capacity configuration, frequent charging and discharging occurred during the participation of the HESS in wind power smoothing, resulting in 11 instances of exceeding the limit for grid-connected power fluctuation on the 1 min scale. Schemes 2 and 3 had optimized capacity configurations, with the numbers of limit exceedances on the 1 min scale reduced to five and four, respectively, and one exceedance on the 10 min scale for both. However, the smoothing effects still failed to reach the ideal level, particularly in terms of their response to sudden fluctuations. Scheme 4 adopted ICEEMDAN for adaptive decomposition of the original wind power and achieved accurate distribution of HESS internal power through IPOA-VMD. It optimized both capacity and power balance, resulting in no limit exceedances on either the 1 min or 10 min scales, fully demonstrating the superiority of the proposed strategy.

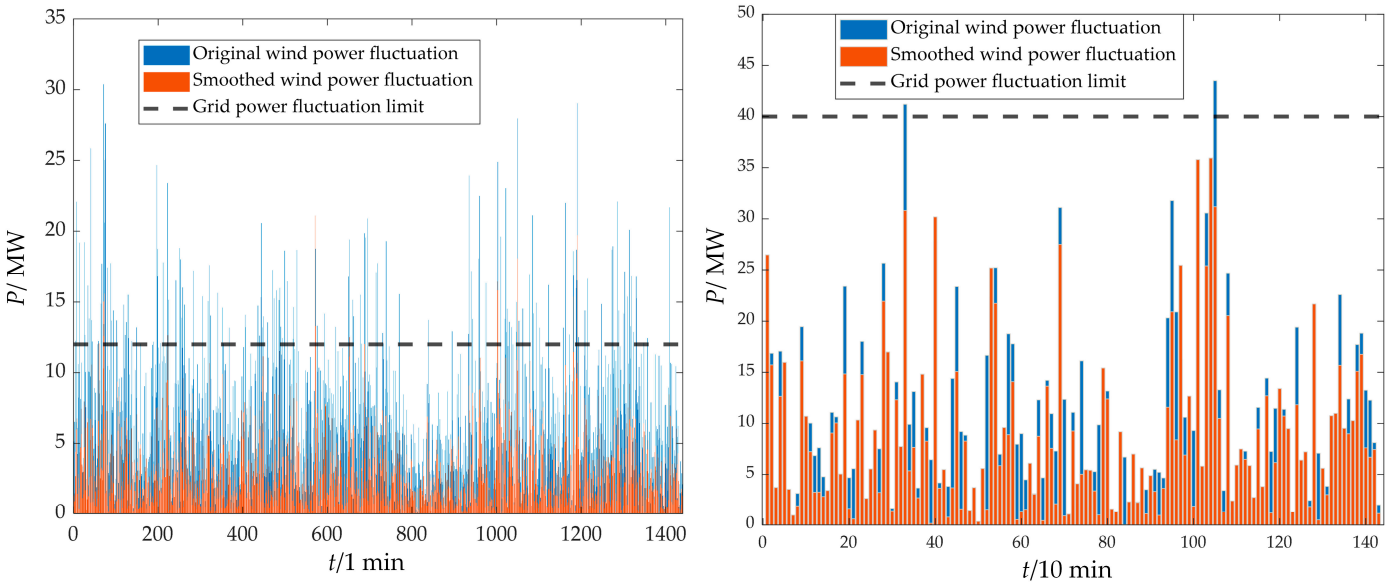

(**a**) (**b**)

Figure 13. The 1 min and 10 min power fluctuations before and after smoothing under scheme 1: (**a**) 1 min; (**b**) 10 min.

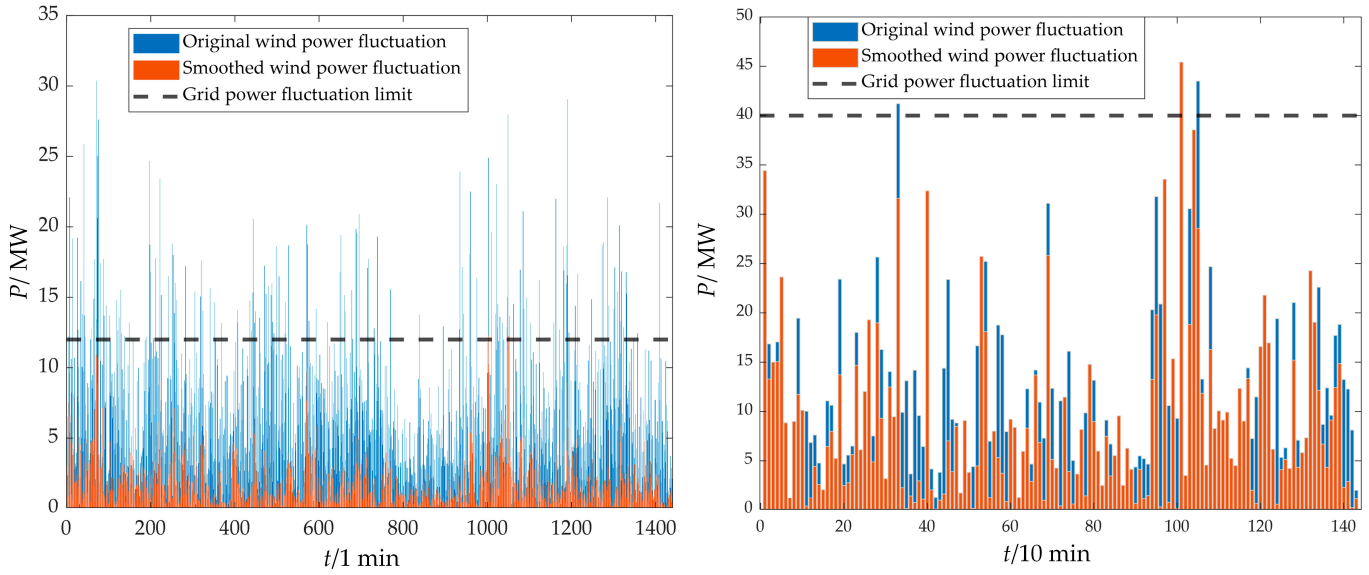

(**a**) (**b**)

Figure 14. The 1 min and 10 min power fluctuations before and after smoothing under scheme 2: (**a**) 1 min; (**b**) 10 min.

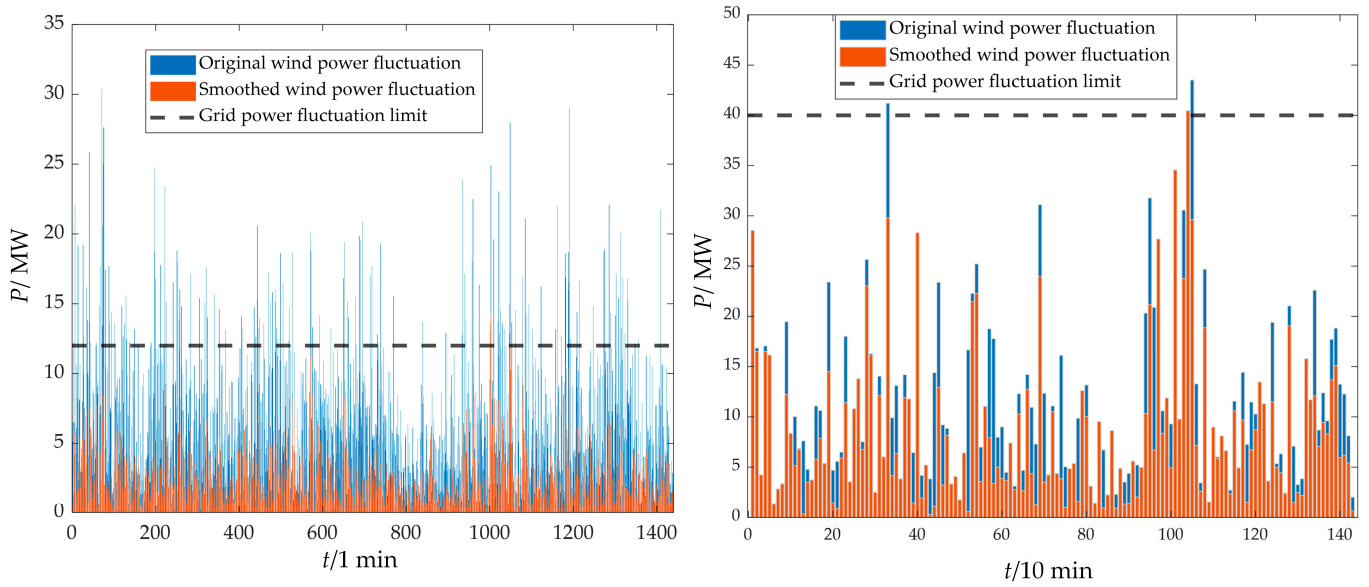

(**a**) (**b**)

Figure 15. The 1 min and 10 min power fluctuations before and after smoothing under scheme 3: (**a**) 1 min; (**b**) 10 min.

Figure 17 compares the output power characteristics of the original grid-connected wind power and the four smoothing schemes. As can be seen from the figure, Scheme 1, based on MA, did not exhibit significant fluctuation suppression, and its smoothed power curve closely matched the original wind power curve. Although Schemes 2 and 3 improved the power fluctuation characteristics to some extent, Scheme 2 showed power compensation overshoot during certain periods, where the smoothed power exceeded the original fluctuation range, potentially leading to grid-connected power limit exceedance risks and additional grid-connected power assessments. In contrast, Scheme 4 used ICEEMDAN for adaptive decomposition of the original wind power, achieving complete extraction of high-frequency components. It then applied the IPOA-VMD to precisely partition the

decomposed modal components and constructed a power allocation strategy based on the dynamic response characteristics of the HESS. It can be clearly seen in the figure that the smoothed power curve of Scheme 4 exhibited optimal smoothing characteristics in the time domain, without any power overshoot. This result validates the effectiveness of the proposed method in meeting the grid-connected power fluctuation standards, significantly improving the grid connection reliability of the wind farm and grid dispatching priority.

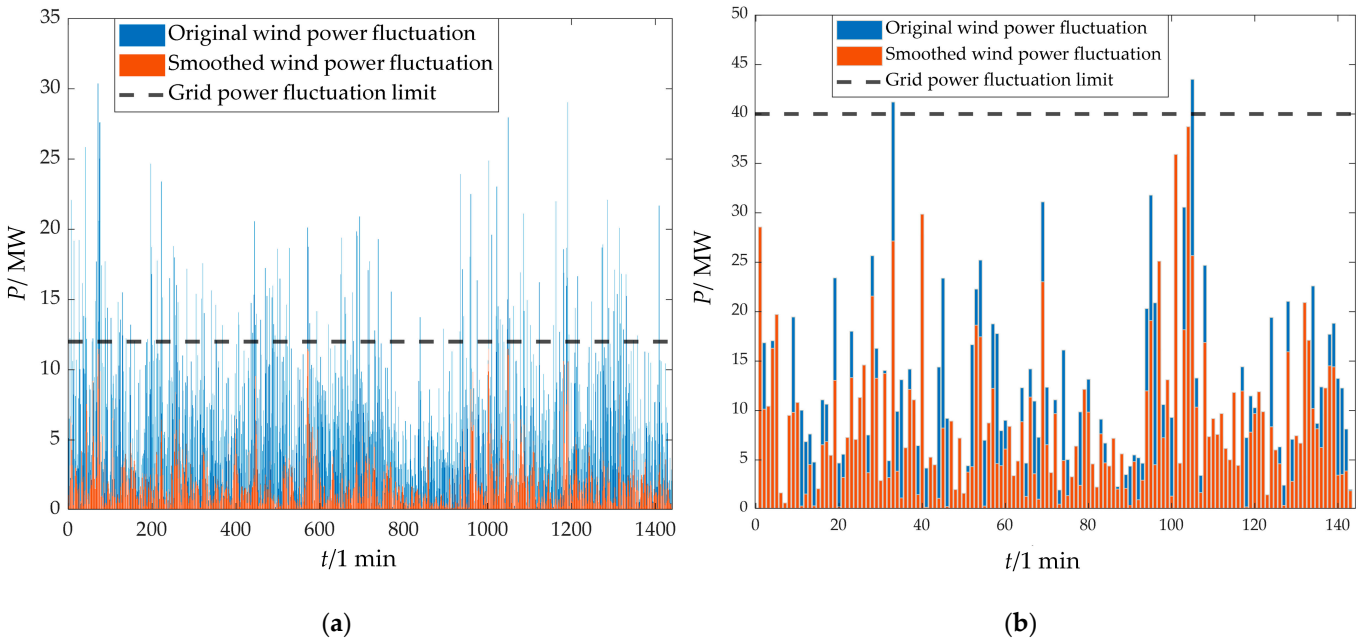

Figure 16. The 1 min and 10 min power fluctuations before and after smoothing under scheme 4: (**a**) 1 min; (**b**) 10 min.

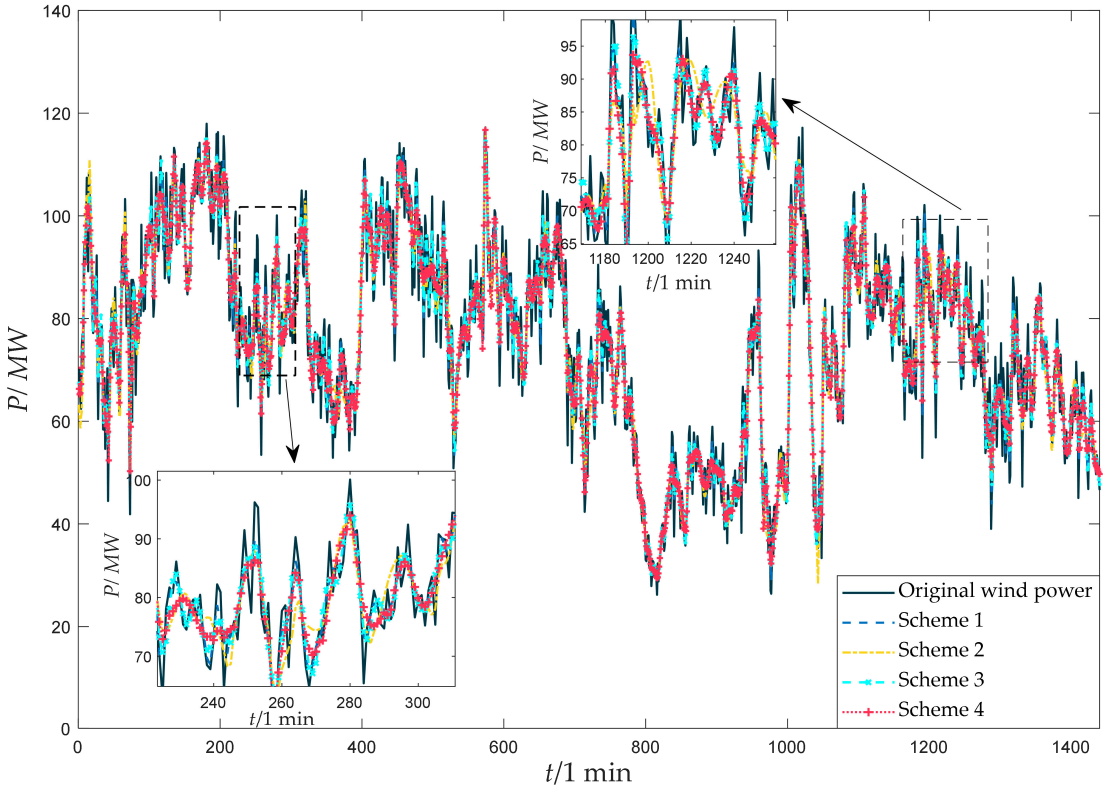

Figure 17. Comparison of grid-connected power curves.

4. Conclusions

In response to the issue of wind power grid-connected fluctuations, this paper proposes a power distribution strategy and capacity optimization method for a HESS based on improved k-means and two-stage decomposition and validated its effectiveness through actual wind farm operational data. The main conclusions are as follows:

1. Compared with traditional PSO and POA, the IPOA was used to optimize the modal number K and quadratic penalty factor α for VMD, performing better in terms of search speed and optimization accuracy. It effectively improved the modal matching accuracy of VMD, enhancing the accuracy of internal power distribution in the HESS.
2. The two-stage decomposition power distribution strategy based on ICEEMDAN and IPOA-VMD could effectively smooth wind power fluctuations, fully utilizing the advantages of power-type and energy-type storage and achieving precise separation of high-frequency and low-frequency components. Through the collaborative compensation of supercapacitors and lithium batteries, the proposed strategy reduced the number of grid-connected power fluctuation exceedances to 0 on both the 1 min and 10 min time scales, improving the wind power fluctuation smoothing effect and optimizing the overall performance of the HESS.
3. k-means++ was used to cluster the annual wind power data by combining SC and DBI, and typical-day data were determined based on the overall characteristics and cumulative fluctuation of each clustering scenario. The case study was conducted based on this, and the results showed that the proposed strategy not only met the grid-connected power fluctuation requirements of wind farms but reduced the overall HESS cost by 7.79% compared with traditional strategies, providing an engineering reference value for HESS capacity planning.
4. The HESS capacity optimization model for smoothing wind power fluctuations established in this study does not consider the impact of dynamic electricity prices and ancillary service revenues on the economic viability of the HESS. Future research is planned involving developing a multiobjective optimization model incorporating demand response and ancillary services to quantify the added value of energy storage participation in the market and further improve the full lifecycle economic analysis.

Author Contributions: Methodology, X.Z. and L.K.; software, X.Z.; validation, L.K., X.W. and Y.L.; data curation, S.H.; writing—original draft preparation, X.Z.; writing—review and editing, L.K.; supervision, L.K., X.W. and Y.L.; project administration, L.K.; funding acquisition, L.K. All authors have read and agreed to the published version of the manuscript.

Funding: This research was funded by the Guangdong Provincial Key Areas R&D Program Funded Projects, grant number NO.2021B0101230003.

Data Availability Statement: The data presented in this study are available on request from the corresponding author due to commercial reasons.

Conflicts of Interest: The authors declare no conflicts of interest.

Appendix A

Table A1. Parameters and values of the IPOA-VMD.

Parameter	N_{pop}	N_{max}	K_b	α_b	tau	DC	init	tol
Value	20	70	[1, 10]	[10, 10,000]	0	0	1	1×10^{-6}

Table A1 Note: N_{pop}: number of pelicans in the population, N_{max}: maximum number of iterations. K_b: upper and lower limits of VMD decomposition levels. α_b: upper and lower bounds of the penalty factor. tau: dual ascent time step (set to 0 to allow noise). DC: determines whether to preserve the DC component (0 fixes the first mode to zero frequency). init: specifies the initial frequency distribution of modes (1 means all initial frequencies are uniformly distributed). tol: tolerance for the convergence criterion.

Table A2. Solver parameter configuration.

Category	Parameter Item	Configuration Value/Description
YALMIP	Version	20180612
	Optimization Model	optimizer function
	Solving Precision	sdpsettings('solver','gurobi+','verbose',2)
	Constraint Tolerance	1×10^{-6}
Gurobi	Version	10.0.1
	MIPGap	0.01
	Maximum Computation Time	3600 s

Table A2 Note: Only a subset of parameters is listed here. All other parameters for the YALMIP toolbox and Gurobi solver used their default values.

Table A3. Parameters and values of the HESS capacity optimization model.

Parameter Name	Value
Unit capacity cost of lithium batteries $c_{Li,E}^{inv}$/[10 k CNY·(MW·h)$^{-1}$]	100
Unit power cost of lithium batteries $c_{Li,P}^{inv}$/[10 k CNY·(MW)$^{-1}$]	150
Unit capacity cost of supercapacitors $c_{sc,E}^{inv}$/[10 k CNY·(MW·h)$^{-1}$]	600
Unit power cost of supercapacitors $c_{sc,P}^{inv}$/[10 k CNY·(MW)$^{-1}$]	100
SOC limit of lithium batteries	[0.2, 0.8]
SOC limit of supercapacitors	[0.1, 0.9]
Discount rate r	5%
Operating lifespan of lithium batteries Y_{Li}/year	5
Operating lifespan of supercapacitors Y_{sc}/year	15
Proportion of O&M costs to investment costs for lithium batteries a_{Li}	2%
Proportion of O&M costs to investment costs for supercapacitors a_{sc}	2%
Residual value rate of lithium batteries b_{Li}	10%
Residual value rate of supercapacitors b_{sc}	20%
Opportunity compensation cost coefficient c_{comp}/[10 k CNY·(MW·h)$^{-1}$]	0.32

References

1. Roga, S.; Bardhan, S.; Kumar, Y.; Dubey, S.K. Recent technology and challenges of wind energy generation: A review. *Sustain. Energy Technol. Assess.* **2022**, *52*, 102239. [CrossRef]
2. Deguenon, L.; Yamegueu, D.; Gomna, A. Overcoming the challenges of integrating variable renewable energy to the grid: A comprehensive review of electrochemical battery storage systems. *J. Power Sources* **2023**, *580*, 233343. [CrossRef]
3. Cui, D.; Jin, Y.; Wang, Y.; Yuan, Z.; Cai, G.; Liu, C.; Ge, W. Combined thermal power and battery low carbon scheduling method based on variational mode decomposition. *Int. J. Electr. Power Energy Syst.* **2023**, *145*, 108644. [CrossRef]
4. Lei, S.; He, Y.; Zhang, J.; Deng, K. Optimal configuration of hybrid energy storage capacity in a microgrid based on variational mode decomposition. *Energies* **2023**, *16*, 4307. [CrossRef]
5. Xinghao, P.; Yanting, L. Wind Power Scenario Generation Method and Application Based onSpatiotemporal Covariance Function. *J. Shanghai Jiaotong Univ.* **2023**, *57*, 1531.
6. Fei, Z.; Yang, H.; Du, L.; Guerrero, J.M.; Meng, K.; Li, Z. Two-stage coordinated operation of A green multi-energy ship microgrid with underwater radiated noise by distributed stochastic approach. *IEEE Trans. Smart Grid* **2024**. [CrossRef]
7. Yang, Z.; Ren, Z.; Li, H.; Sun, Z.; Feng, J.; Xia, W. A multi-stage stochastic dispatching method for electricity-hydrogen integrated energy systems driven by model and data. *Appl. Energy* **2024**, *371*, 123668. [CrossRef]
8. Wang, Y.; Liu, Y.; Kirschen, D.S. Scenario reduction with submodular optimization. *IEEE Trans. Power Syst.* **2016**, *32*, 2479–2480. [CrossRef]
9. Wu, A. Capacity Optimization Configuration of Energy Storage System in Wind Farm Based on Sand Cat Swarm Algorithm. In Proceedings of the 2023 Asia Conference on Power, Energy Engineering and Computer Technology (PEECT), Qingdao, China, 21–23 July 2023; pp. 12–17.
10. Tiejiang, Y.; Yang, Y.; Rui, L.; Dongfang, J. Optimized Configuration of Hydrogen-Energy Microgrid Capacity Considering Source Charge Uncertainties. *Electr. Power* **2023**, *56*, 21–32.
11. Zhang, Y.; Pan, G.; Chen, B.; Han, J.; Zhao, Y.; Zhang, C. Short-term wind speed prediction model based on GA-ANN improved by VMD. *Renew. Energy* **2020**, *156*, 1373–1388. [CrossRef]
12. Lixiang, H.; Xinyan, Z.; Shuai, L.; Rui, S.; Shiqiang, L.; Guanghao, Z. Hybrid Energy Storage Power Distribution Strategy for Smoothing Wind-Photovoltaic Power Fluctuation. *Sci. Technol. Eng.* **2023**, *23*, 10825–10834.

13. Long, C.; Fanghua, Z. Wavelet Transform Method for Hybrid Energy Storage System Smoothing Power Fluctuation. *Electr. Power Autom. Equip./Dianli Zidonghua Shebei* **2021**, *41*, 100–104+128.
14. Kunhua, J.; Yun, W.; Lina, D.; Yao, Z. Hybrid Energy Storage Wind Power Smoothing Control Strategy for Improving Bidirectional Regulation Ability. *Smart Power* **2024**, *52*, 55–62.
15. Ren, Y.; Suganthan, P.N.; Srikanth, N. A comparative study of empirical mode decomposition-based short-term wind speed forecasting methods. *IEEE Trans. Sustain. Energy* **2014**, *6*, 236–244. [CrossRef]
16. Lin, L.; Zhu, L.; Yang, R.; Gao, Y.; Wu, Q. Capacity optimization of hybrid energy storage for smoothing power fluctuations based on spectrum analysis. In Proceedings of the 2017 2nd International Conference on Power and Renewable Energy (ICPRE), Chengdu, China, 20–23 September 2017; pp. 61–65.
17. Qing, Z.; Xinran, L.; Ming, Y.; Yijia, C.; Peiqiang, L. Capacity Determination of Hybrid Energy Storage System for Smoothing Wind Power Fluctuations with Maximum Net Benefit. *Trans. China Electrotech. Soc.* **2016**, *31*, 40–48.
18. Zhang, Y.; Zhao, F. Optimal configuration of wind storage capacity based on VMD and improved GWO. *J. Phys. Conf. Ser.* **2022**, *2378*, 012048. [CrossRef]
19. Zhang, Y.; Pan, Z.; Wang, H.; Wang, J.; Zhao, Z.; Wang, F. Achieving wind power and photovoltaic power prediction: An intelligent prediction system based on a deep learning approach. *Energy* **2023**, *283*, 129005. [CrossRef]
20. Arthur, D.; Vassilvitskii, S. *k-means++: The Advantages of Careful Seeding*; Stanford: Palo Alto, CA, USA, 2006.
21. Miraftabzadeh, S.M.; Colombo, C.G.; Longo, M.; Foiadelli, F. K-means and alternative clustering methods in modern power systems. *IEEE Access* **2023**, *11*, 119596. [CrossRef]
22. Maulik, U.; Bandyopadhyay, S. Performance evaluation of some clustering algorithms and validity indices. *IEEE Trans. Pattern Anal. Mach. Intell.* **2002**, *24*, 1650–1654. [CrossRef]
23. Poongadan, S.; Lineesh, M. Non-linear Time Series Prediction using Improved CEEMDAN, SVD and LSTM. *Neural Process. Lett.* **2024**, *56*, 164. [CrossRef]
24. Dragomiretskiy, K.; Zosso, D. Variational mode decomposition. *IEEE Trans. Signal Process.* **2013**, *62*, 531–544. [CrossRef]
25. Trojovský, P.; Dehghani, M. Pelican optimization algorithm: A novel nature-inspired algorithm for engineering applications. *Sensors* **2022**, *22*, 855. [CrossRef]
26. Pareek, N.K.; Patidar, V.; Sud, K.K. Image encryption using chaotic logistic map. *Image Vis. Comput.* **2006**, *24*, 926–934. [CrossRef]
27. Jin, Z.; He, D.; Wei, Z. Intelligent fault diagnosis of train axle box bearing based on parameter optimization VMD and improved DBN. *Eng. Appl. Artif. Intell.* **2022**, *110*, 104713. [CrossRef]
28. Li, Z.; Zhao, H.; Lin, Y. Multi-task convolutional neural network with coarse-to-fine knowledge transfer for long-tailed classification. *Inf. Sci.* **2022**, *608*, 900–916. [CrossRef]
29. Qu, H.; Ye, Z. Comparison of Dynamic Response Characteristics of Typical Energy Storage Technologies for Suppressing Wind Power Fluctuation. *Sustainability* **2023**, *15*, 2437. [CrossRef]
30. Xiong, X.; Rengang, Y.; Lin, Y.; Jianlin, L. Economic Evaluation of Large-Scale Energy Storage Allocation in Power Demand Side. *Trans. China Electrotech. Soc.* **2013**, *28*, 224–230.
31. Suhua, L.; Tianmeng, Y.; Yaowu, W.; Yongcan, W. Coordinated Optimal Operation of Hybrid Energy Storage in Power System Accommodated High Penetration of Wind Power. *Autom. Electr. Power Syst.* **2016**, *40*, 30–35.